The photomultiplier ports are blanked off for transport and testing. Also visible in Fig. VII.2 are the belly band (in solid black) and 4 supports forming one half of a cradle-like structure. The end view of this segment on the bottom of Fig. VII.2 is similar to that shown in the drawing of Fig. IV.2. One observes a large cylindrical opening in the center, meant to accommodate the scattering chamber, and two pairs of duct pipes (halves) extending radially outwards, as well as the vertical half sleeve for the 8" chamber support and pumping pipe at the bottom half of the segment.

In Fig. VII.3, segment 1, the backward conical end segment, is depicted in two slightly different views. Here, the geometry of the ladder-like double support structure with buttress and base plates of the undercarriage is seen clearly. The rollers are not attached yet. Scintillator inlet and outlet pipes are seen protruding horizontally out of the left side of the tank.

Prior to final assembly of the individual tank segments, i.e., with one of the end lids not yet welded to the rest of the tank body, the inside tank surfaces were thoroughly cleaned with organic solvents. Subsequently, they were prepared for mounting of the Teflon reflector sheets, which had been precut to form a mantle of the tank interior surface. These Teflon sheets were pushed over stainless-steel studs, which had been point-welded to the tank surfaces, and held in place by fast-lock stainless-steel washers. This method results in effectively reflecting surfaces, with only relatively small fractions covered by the flat washers. This is demonstrated in Fig. VII.4, showing two views of the interior of segment 3, as seen through one of its ports. After mounting of the reflectors on all inner surfaces of a given tank segment, the spherical or circular end piece was welded to the remainder of the tank. As observed in welding tests of stainless steel with Teflon sheets attached, the Teflon discolors only in the vicinity of the welds. Therefore, this procedure does not affect the highly reflective quality of the inner tank surfaces significantly.

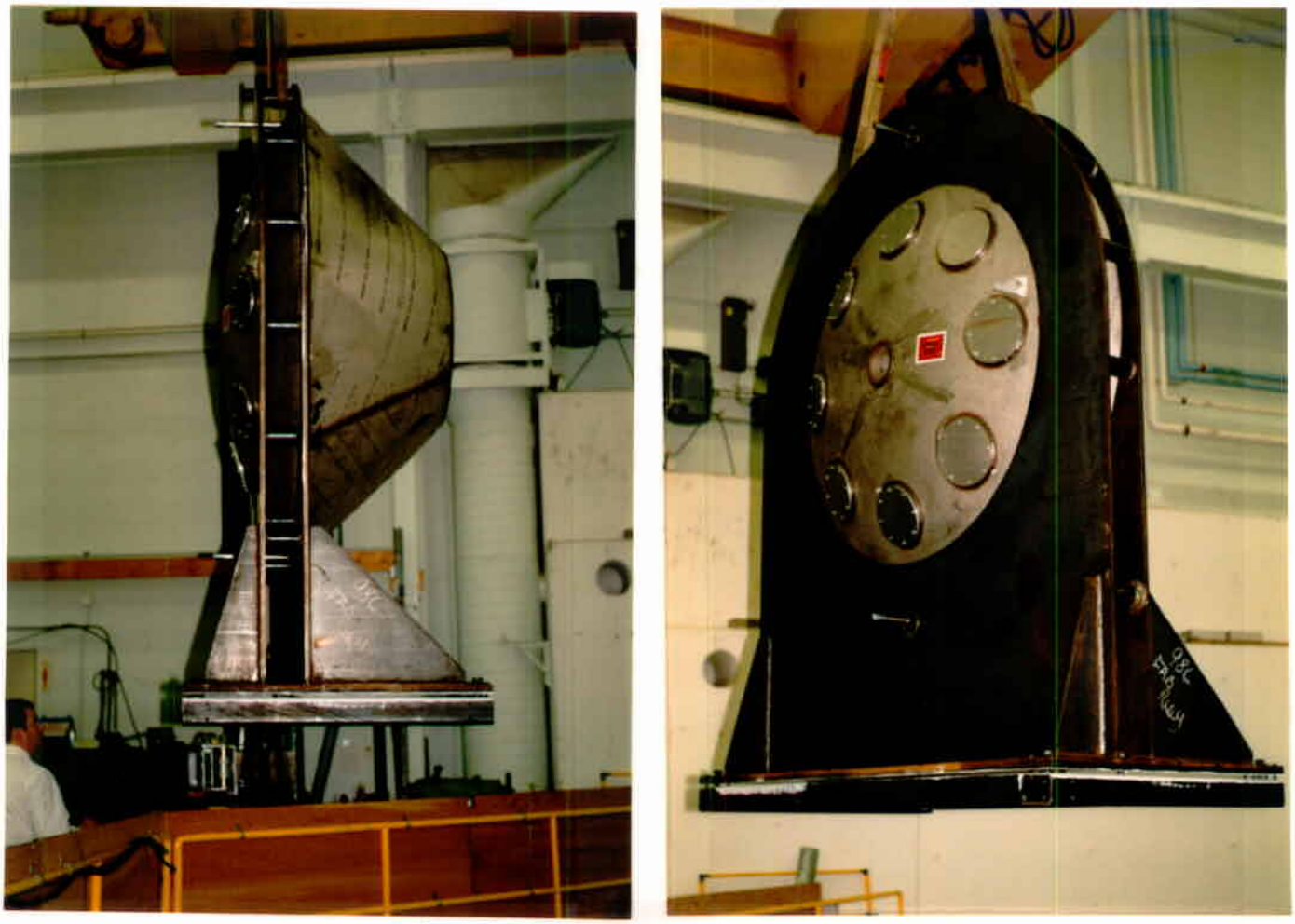

**Fig. VII.3:** Segment 1, the backward conical end segment, is depicted in two slightly different views.

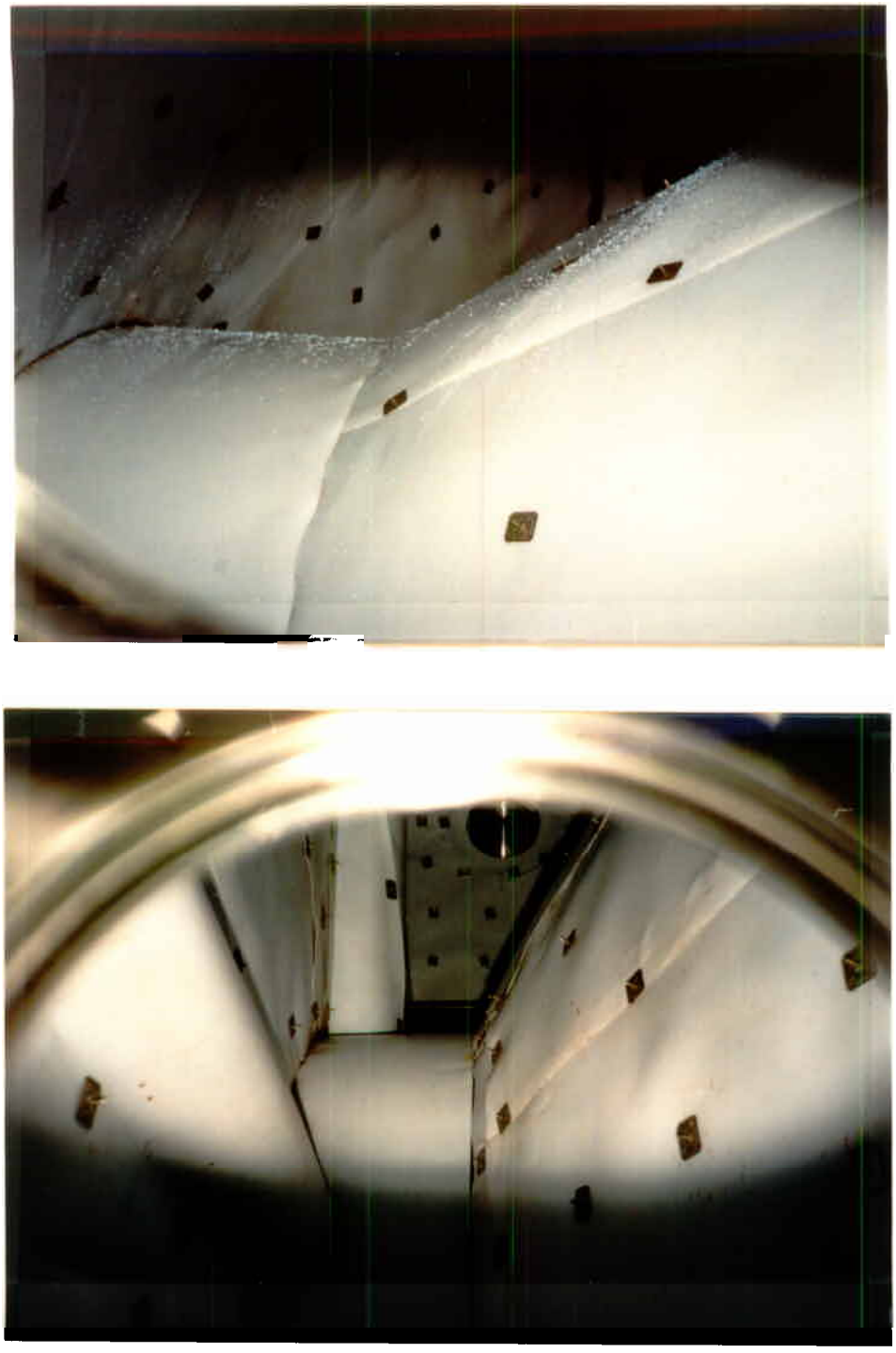

**Fig. VII.4:** Two views of the interior of segment 3, as seen through one of its ports. Teflon sheets are visible, which are affixed to the inner tank walls by stainless-steel studs and fast-lock washers.

After complete assembly and welding of the *SuperBall* tanks, the photomultiplier ports were closed hermetically with blank aluminum flanges, and each tank was pressure tested with air at 5 psi. These air tests were performed at *Fab-Alloy* plant on August 10, 1993. All parts of the *SuperBall* made of carbon steel were primed to protect the surfaces from corrosion.

An area in the S-2 vault at MSU/NSCL was designated and prepared for the *SuperBall* occupancy. A 12-cm high steel-channel safety dam was cemented enclosing the space to be taken by the detector and the additional maintenance tank, forming a containment vessel. The concrete bottom and walls of this structure were painted with a chemically inert epoxy paint, preventing exposure of concrete to the scintillator liquid, should it ever leak out of the detector. The *SuperBall* rails were welded together, aligned horizontally and with the beam line. After height adjustment and leveling, the rails were cemented into place.

Figs. VII.5 and 6 show different phases of the installation of the *SuperBall* in its present location in the NSCL S-2 vault, photographed on September 15, 1993. In these figures, beam entrance is on the right. For example, on the right-hand side of Fig. VII.5, segments 5, 4, and 3 are seen in their locked position, separated from the upstream section 1, and section 2 is seen suspended over the gap to be lowered into position. In Fig. VII.6, the *SuperBall* is seen with its segments separated (bottom) and partially closed (top).

After mounting of the rollers and installation on its tracks, the detector was leak tested by filling all tanks with water, and full mechanical functionality of the tank assembly was ascertained. Every tank segment was found movable on the rails if manually pushed or pulled by 2-3 persons. Then, the scattering chamber was installed on its support between the rails. It is depicted in Fig. VII.7, opened on the beam-upstream side. Clearly distinguishable in this figure are the aluminum main chamber ring with two ports armed with cable feed-throughs. The downstream stainless-steel dome is still attached to

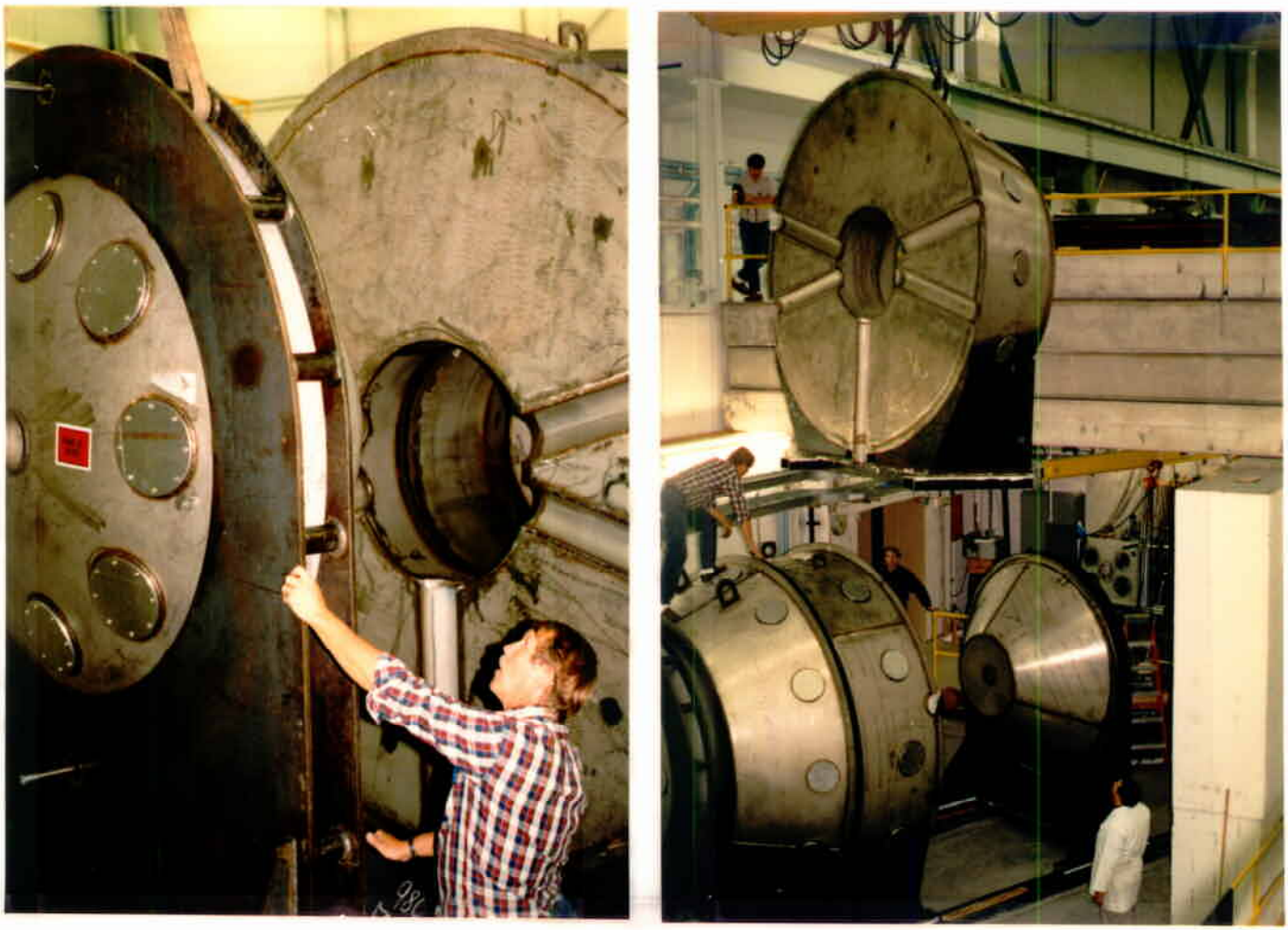

**Fig. VII.5:** Installation of the *SuperBall* in the NSCL S-2 vault, photographed on September 15, 1993. Segments 5, 4, and 3 are seen in their locked position, separated from the upstream segment 1, and segment 2 is seen suspended over the gap to be lowered into position. The beam entrance is on the right.

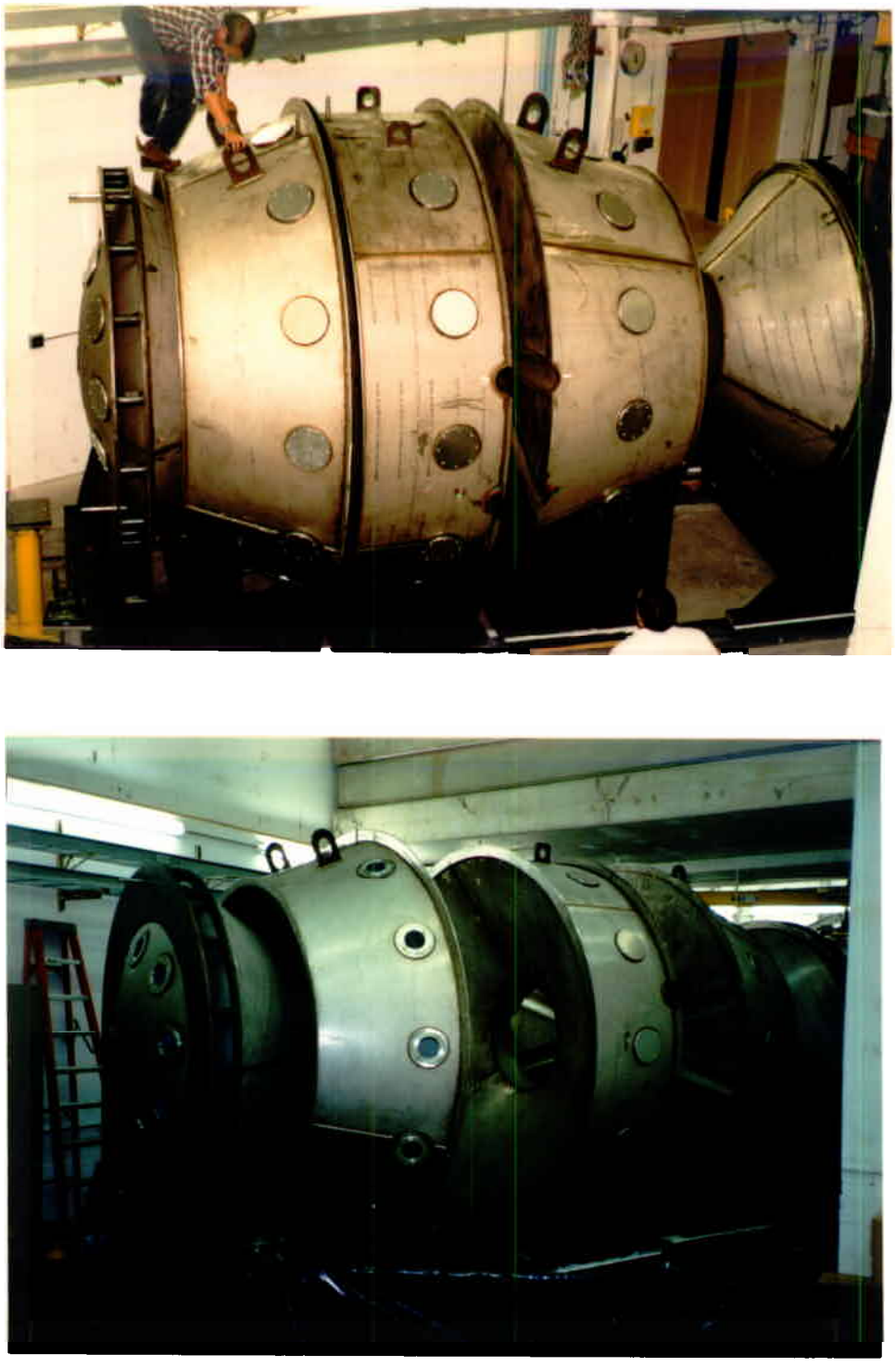

**Fig. VII.6:** Installation of the *SuperBall*. The *SuperBall* is seen with its segments separated (bottom) and partially closed (top).

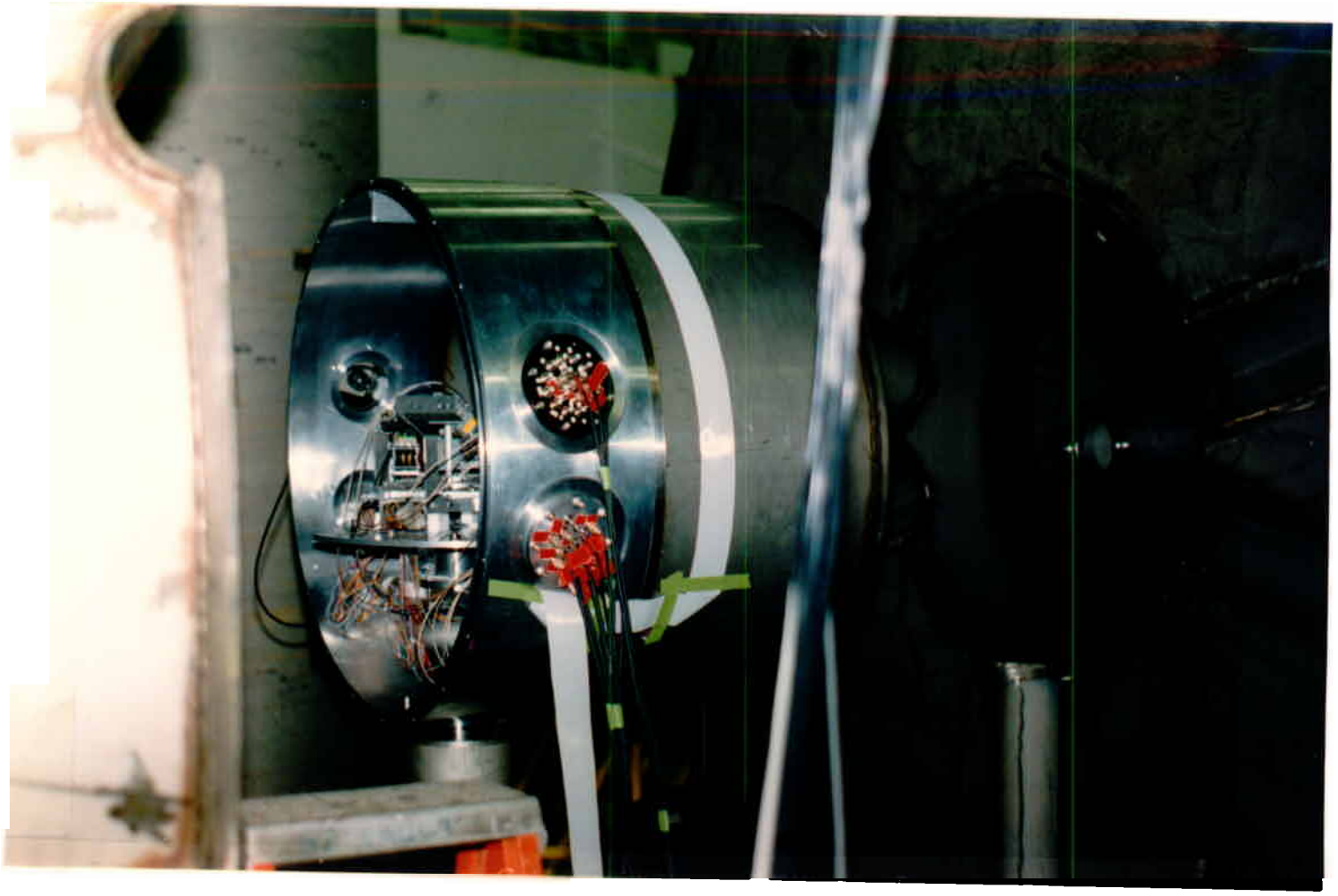

**Fig. VII.7:** The *SuperBall* scattering chamber with its upstream dome removed.

the chamber. On the right-hand side, the opening of segment 3 is visible, which accepts the chamber.

Following the water tests, the tank interiors were left to dry on air. Final cleaning of the tank interiors was accomplished by flushing and spraying the walls with trimethyl-benzene, the solvent that forms the basis of the *SuperBall* scintillator liquid. This procedure was followed by a replacement of the blank aluminum flanges used to close the photomultiplier ports by the window flanges, and the hookup of the scintillator overflow vessels to the outlet pipes on the top of the tank segments. The glass window allowed a visual inspection of the filling of the tanks with scintillator. Care was taken during the cleaning and the transfer of the 16,000 *l* of scintillator from individual, 55-gal PVC drums into the *SuperBall* tanks, to avoid escape of trimethyl-benzene fumes into the environment of the laboratory. The scintillator liquid was filled into the tanks from the bottom using a *Warren Sandpiper Pump*, purchased from *Siewert Equipment Co. TgR-1A*, connected via Teflon hoses and stainless-steel quick-connect valves to the bottom inlets of the tanks. In this first filling, small air bubbles remained at the top of tanks 2-4. The filling took about two days and was completed during the week of December 6, 1993.

Finally, the photomultipliers were mounted onto the window flanges, with their magnetic shields, housings and bases. Fig. VII.8 shows the fully assembled *SuperBall* in a configuration where the scattering chamber can be serviced. Here, the overflow vessels for tanks 3-5 are seen mounted on the corresponding undercarriages. These vessels are also made of stainless steel and carry aluminum flanges Also visible in the foreground is the upright cylindrical maintenance tank. An aluminum flange is mounted on its top dome, carrying a pressure gauge and several hose connectors. The schematical drawing of Fig. VII.9 shows the *SuperBall* in closed configuration on its track in the S-2 cave at the NSCL. The hatched areas denote concrete shielding. Rectangles with diagonals indicate the massive iron shielding. This includes a cylindrical piece mounted at the beam dump shown on the right. Not shown are a pumping station with turbo and roughing pumps at

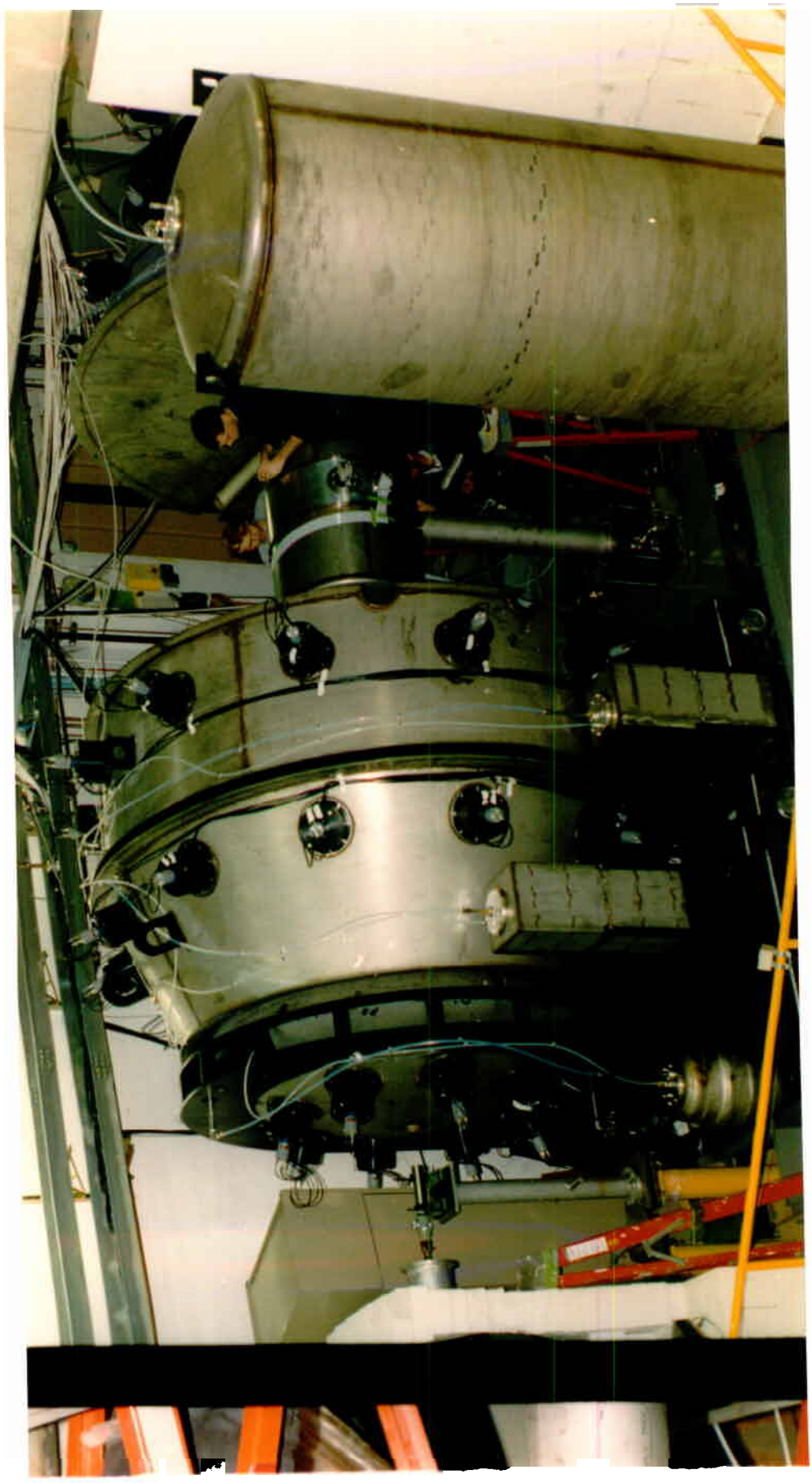

**Fig. VII.8:** Fully assembled *SuperBall* in a configuration where the scattering chamber can be serviced. The overflow vessels for tanks 3-5 are seen mounted on the corresponding undercarriages. Also visible in the foreground (right) is the maintenance tank.

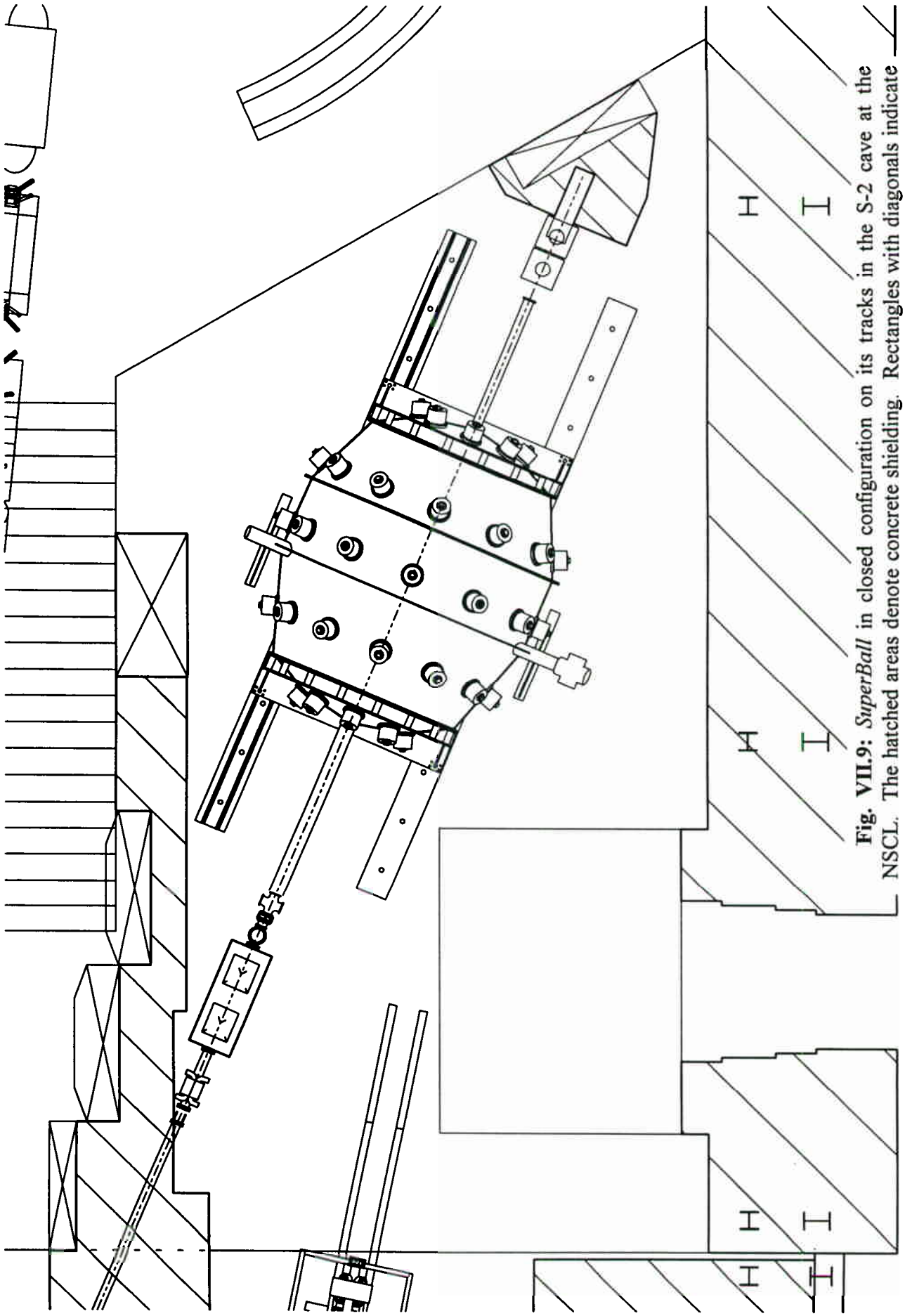

**Fig. VII.9:** *SuperBall* in closed configuration on its tracks in the S-2 cave at the NSCL. The hatched areas denote concrete shielding. Rectangles with diagonals indicate massive iron shielding. This includes a cylindrical piece mounted at the beam dump shown on the right. Not shown is a pumping station with turbo and roughing pumps at the beam entrance of the *SuperBall*. The maintenance tank, also not shown in this figure, is located in the upper right corner of the enclosure.

the beam entrance of the *SuperBall* and the safety dam . The maintenance tank, also not shown in this figure, is located in the upper right corner of the enclosure.

## VIII. Detector Performance Tests

The first electronic signals from the *SuperBall* were observed on December 10, 1993. The detector was found to perform according to the design goals. Off-line test measurements were performed with radioactive sources placed at various positions on the five tank segments, in order to study the response of each segment separately. All segments were found to function satisfactorily. As expected, the signals were largest from the conical end segments 1 and 5, with the simplest internal geometry and, hence, the best light collection efficiency. The relatively smallest pulse heights came from tank 4, formed of three coaxial cones. The light output spectra from individual photomultipliers of a given tank were matched to one another, by varying the applied high voltage, in order to achieve a response as uniform over the tank as possible. For this purpose, radio-active $\gamma$-ray and $^{252}Cf$ fission sources were placed in the center of each segment. The individual tests will be continued in an attempt to further optimize the performance of the *SuperBall*.

First calibration data taken with the whole detector are presented in Fig. VIII.1. These data were taken with a very weak $^{252}Cf$ fission-neutron source in the center of the *SuperBall*, i.e., in target position. A Si detector mounted close to the $^{252}Cf$ fission source provided the trigger for the *SuperBall* measurement. The top part of Fig. VIII.1 shows the prompt light output spectrum of the neutron detector, obtained by summing all tank signals. The origin of light output scale of this spectrum, taken with a charge-to-digital converter (QDC), is shifted approximately to channel 200, due to the well-known "pedestal" effect. One observes a bump around channel 300 due to fission neutrons and $\gamma$-

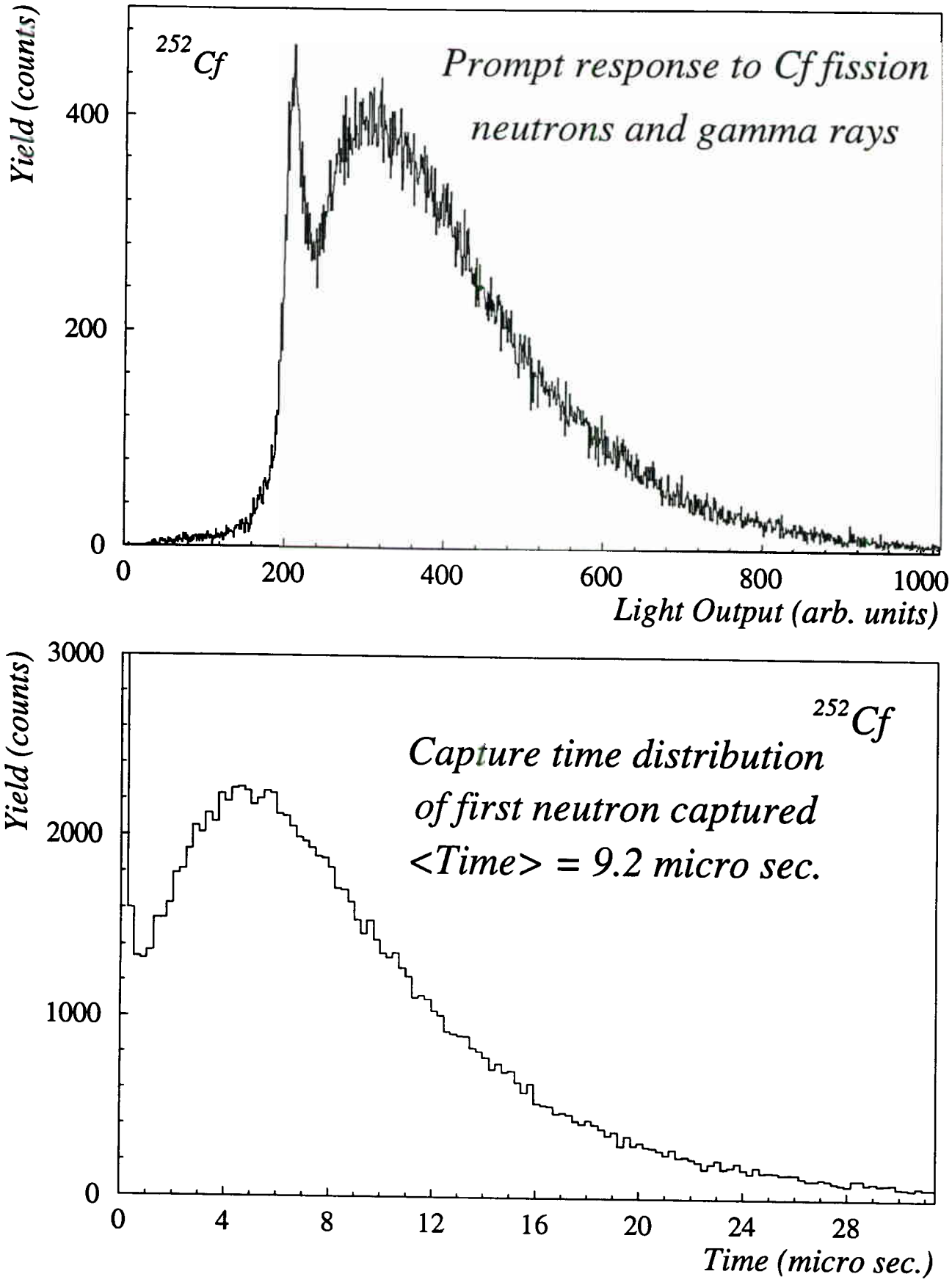


**Fig. VIII.1:** The prompt light output spectrum of the neutron detector, obtained by summing all tank signals, is shown on top. The origin of the spectrum is shifted approximately to channel 200, due a QDC "pedestal" effect. The capture time distribution of the first neutron is depicted at the bottom.

rays, corresponding to approximately 10-12 MeV. The sharp peak on its left is due to a cutoff of the noise spectrum at small pulse heights.

The capture time distribution of the first neutron is depicted on the bottom of Fig. VIII.1. The distribution shows a well developed peak at about 5 μs after a $^{252}$Cf fission event and has a tail stretching over a time interval of many μs, bringing the average capture time up to 9 μs. When comparing this experimental capture time distribution to that of Fig III.3, one has to keep in mind that the theoretical distribution is only for a single neutron, while experimentally, one measures the capture time of the first out of an average of 3.8 fission neutrons. In fact, simulation calculations show that the two distributions are well consistent with one another. The shape of the experimental distribution with a pronounced maximum is indicative of proper functioning of the detector and adequate counting rates. At tank event rates of more than a few times $10^3 s^{-1}$, the valley, visible in Fig. VIII.1 at small times, begins to fill in, and event mixing starts to take place. Then, the proper origin of a light flash seen by the detector cannot be determined. For the *SuperBall*, mixing between true $^{252}$Cf fission events and background events becomes important. Because of its size, the *SuperBall* detects cosmic radiation and other environmental background at rates of the order of $10^4 s^{-1}$, resulting in an average multiplicity of background events of the order $\langle m_b \rangle$ = 3-4. The effect of the background can be reduced by narrowing the window of acceptance of the light output pulse height spectrum. This, however, generally reduces also the efficiency of neutron detection. Although relatively high, the background is not expected to cause problems in heavy-ion reactions at intermediate bombarding energies, where neutron multiplicities are high.

Effect and background in a measurement of the $^{252}$Cf fission neutron multiplicity distribution are illustrated in Fig. VIII.2, for an electronic threshold of 1-2 MeV on the light output spectrum. The top portion of this figure depicts the measured distribution of the event multiplicity, true neutron captures and background events combined, with the unnormalized probability (yield) on a logarithmic scale, plotted *vs* multiplicity. This combined multiplicity is, obviously, not Gaussian distributed. The average event multiplicity

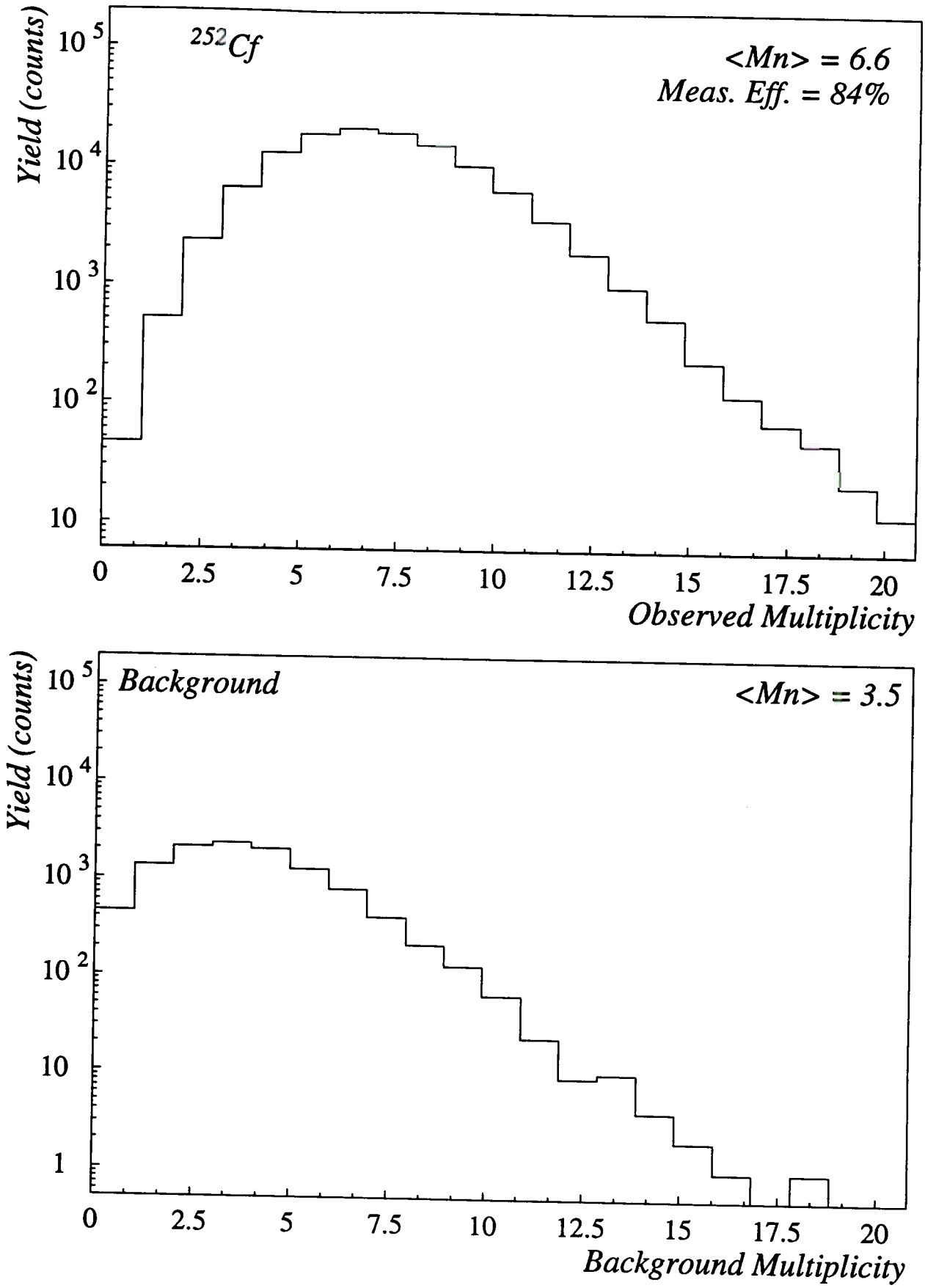


**Fig. VIII.2:** The top portion depicts the total measured distribution of the event multiplicity, while the multiplicity distribution of just background events is shown in the lower portion.

is $\langle m_{e+b} \rangle = 6.6$, and the distribution has an exponential tail. This is largely due to the multiplicity distribution of background events shown in the lower portion of Fig. VIII.2. It corresponds to a mean multiplicity of $\langle m_b \rangle = 3.5$ that should be subtracted from the above value of $\langle m_{e+b} \rangle$ to determine the multiplicity $\langle m_e \rangle$ associated with the effect alone. Using the literature value [Van73] for the $^{252}$Cf fission neutron multiplicity, one deduces an efficiency of $\varepsilon \approx 0.84$ for the *SuperBall* for these neutrons in the test setup. It should be noted that the above background multiplicity is a function of the duration of the counting gate, which in this measurement had the maximum value of 128 $\mu s$. It is possible, to reduce the gate duration by a factor of the order of two, increasing the true multiplicity-to-background ratio by approximately the same factor.

The first in-beam tests were performed in a one-day experimental run on December 28/29, 1993, followed by a second test experiment on Feb. 2, 1994, where a series of Al, Ag, and Bi targets were bombarded with a $^{136}$Xe beam of energy E/A = 28 MeV. In April 1994, the *SuperBall* was run in conjunction with the St. Louis *MicroBall* $4\pi$ charged-particle array, in an experiment studying the reaction $^{197}$Au+$^{86}$Kr at E/A = 35 MeV. In the most recent experiment, performed in March 1995, the symmetric systems $^{112}$Sn +$^{112}$Sn and $^{124}$Sn +$^{124}$Sn were measured at E/A = 40 MeV with a configuration in which the *SuperBall* contained in its internal scattering chamber a rather complex array of charged-particle detectors, including the MSU *Miniball*, the St.Louis *MiniWall*, and a new Si-strip/CsI position-sensitive detector a forward angles.

The functionality of the *SuperBall* in these experiments is well demonstrated by the capture time distributions of 10 successive neutrons of ensembles of neutrons emitted in events of $^{112}$Sn +$^{112}$Sn collisions at E/A = 40 MeV. These distributions are shown in Fig. VIII.3, with the neutron number increasing from left to right and from top to bottom. One observes from this figure, that the capture time distribution for the first neutron is well peaked (at about 8 $\mu$s). For higher neutron numbers, the most probable capture time increases, and the time distribution broadens, until for $n \geq 9$, the peak disappears completely, and the distribution increases monotonically with time. The rate of change of the

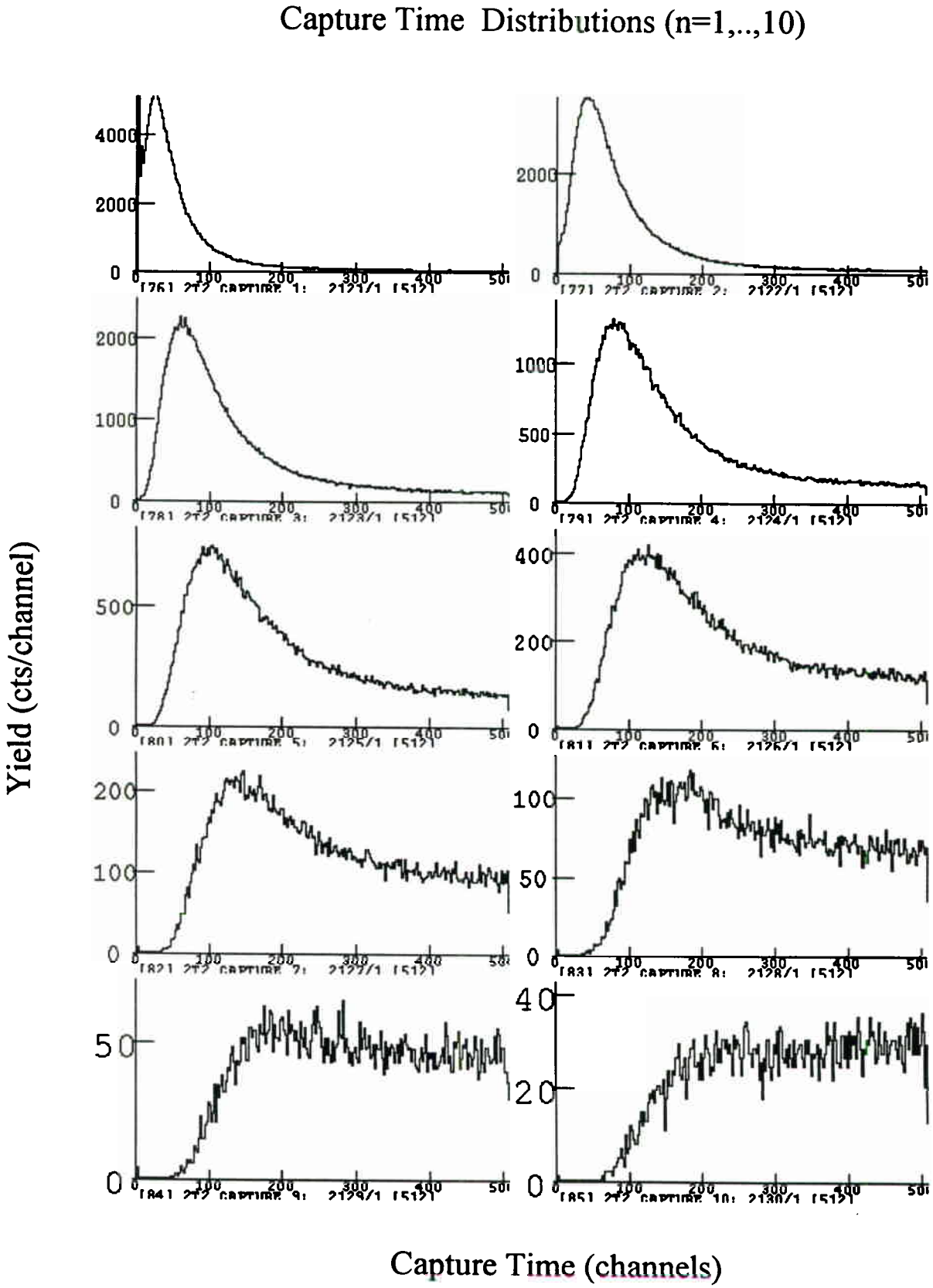


**Fig. VIII.3:** Capture time distributions for successive neutrons, as measured for the $^{112}$Sn +$^{112}$Sn reaction (E/A=40 MeV) with *SuperBall* segment 2. The neutron number increases from left to right and from top to bottom.

capture time distribution wit neutron number depends strongly on the number of neutrons detected in an event. For large neutron multiplicities, the time distribution becomes very compressed. This behavior is expected from the statistical counting arguments presented in the context of the discussion of eq. III.2.

Fig. VIII.4 represents some of the data taken in the experiment, where Al, Ag, and Bi targets were bombarded with a $^{136}$Xe beam of energy E/A = 28 MeV, mentioned previously. These data are well understood and demonstrate again the proper functioning of the *SuperBall* under actual running conditions. Each of the three panels in this figure shows the observed total multiplicity plotted *vs* the summed light output, for events in which a massive reaction product was detected in coincidence with a Si telescope at an angle of 3.5$^{o}$. The horizontal ridge appearing in each of the panels at low light outputs is an instrumental artifact due to random triggering. The correlation between prompt light output and multiplicity is rather well defined for the $^{209}$Bi+$^{136}$Xe reaction illustrated in the lowest panel. As expected, one observes an increase in light output with increasing multiplicity. This is so because of the increases in both average kinetic energy and multiplicity of the neutrons evaporated from a compound nucleus, as the excitation energy of that nucleus is raised. The correlation is somewhat non-linear, perhaps due to the drop in capture probability with increasing neutron energy. In addition, the slope of the light-output-*vs*-multiplicity correlation decreases with decreasing mass of the target. This effect is well understood for a dissipative reaction, in which there are only two primary massive fragments produced in the first step of the reaction. In a second step, the excited primary fragments decay via evaporation of neutrons and light charged particles, or by fission. Charged-particle emission is hindered by the large Coulomb barriers for emission that are characteristic of fragments with high atomic numbers *Z*. Then, for a heavy system, neutrons dominate the evaporation process, from low to high excitation energies, and the average neutron kinetic energy (measured by the scintillator light output) is relatively low. If, on the other hand, the primary reaction products are relatively small, with small Coulomb barriers, charged-particle emission competes more effectively with neutron

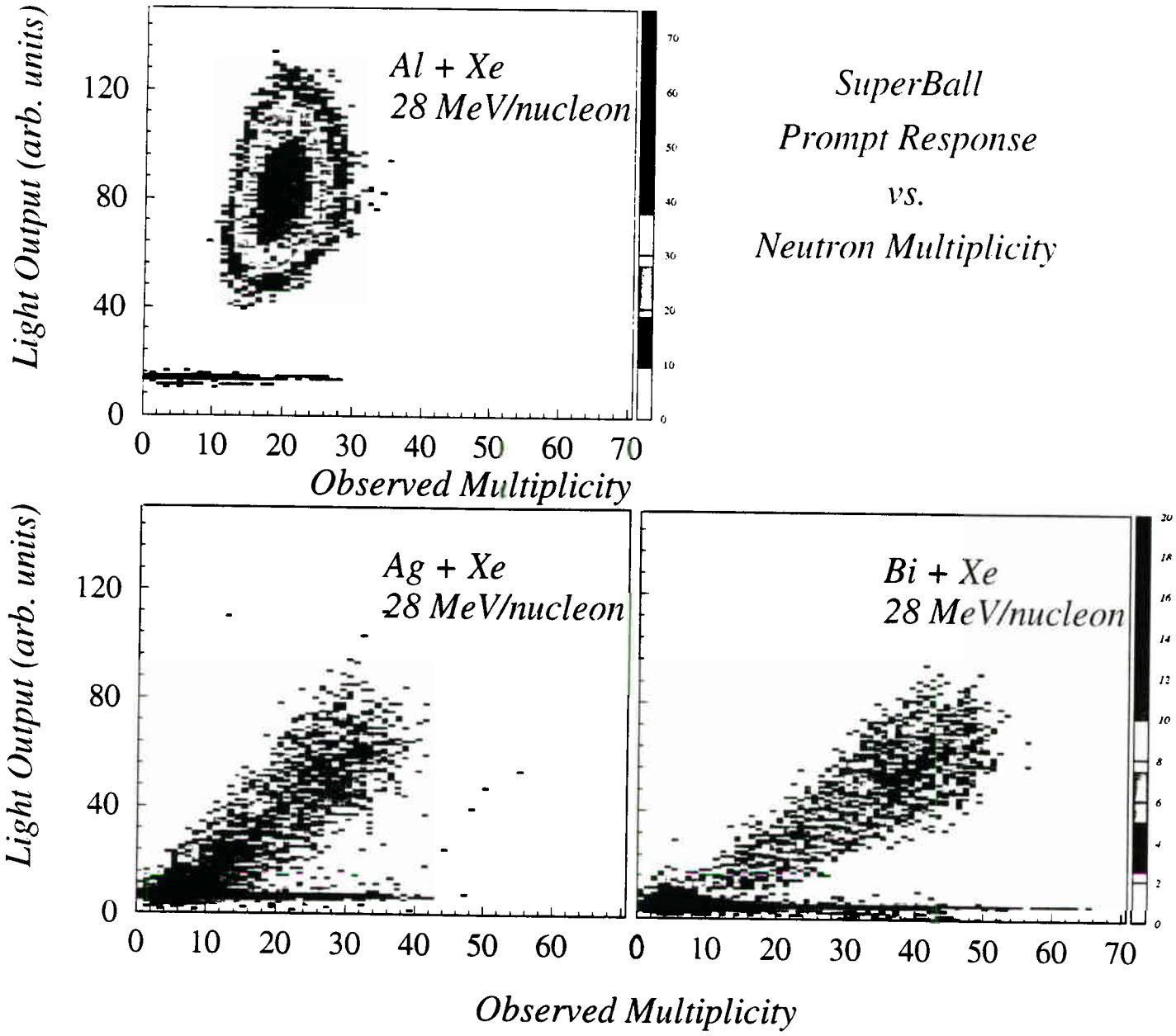


**Fig. VIII.4:** Results of early in-beam tests (Feb. 2, 1994), with a $^{136}$Xe beam of energy E/A = 28 MeV bombarding Al, Ag, and Bi targets. For each target, the observed total multiplicity plotted *vs* the summed light output, for events in which a massive reaction product was detected in coincidence with a Si telescope at an angle of 3.5°.

evaporation, reducing the average neutron multiplicity but increasing the average kinetic energy of these neutrons.

One also expects that, with increasing excitation, the neutron spectrum broadens, leading to a broader multiplicity distribution [Sch80]. This correlation is indeed observed in the lowest panel of Fig. VIII.4, which shows the yield ending in a bump at high multiplicities and light outputs, which is broader than the width of the rest of the ridge. The same features are observed in the middle panel of Fig. VIII.4 illustrating results for the $^{109}$Ag+$^{136}$Xe reaction. The $^{27}$Al+$^{136}$Xe, inverse-kinematics reaction, shown at the top of this figure, is represented only as a broad bump. This is expected, because the lower portion of the ridge is associated with quasi-elastic and partially damped events, where the associated relatively cold fragments are emitted at very small angles and do not reach the trigger telescope.

The data exhibited in Fig. VIII.5 are for the same four $^{136}$Xe-induced reactions discussed above. They show the difference in response of the individual *SuperBall* tank segments to the differing kinematical conditions of a reaction, going from a more isotropic angular distribution of neutrons, as expected for the $^{209}$Bi+$^{136}$Xe and $^{109}$Ag+$^{136}$Xe reactions, to the highly forward-focused distribution expected from the inverse-kinematics reaction $^{27}$Al+$^{136}$Xe. This feature is shown in Fig. VIII.5, where the observed neutron multiplicity is plotted *vs* the *SuperBall* segment number defining coarse bins in laboratory angle. The strong forward peaking in the neutron angular distribution is clearly seen in the case of the $^{27}$Al+$^{136}$Xe reaction, whereas the angular distributions are relatively flat for the heavier targets.

In its first production experiment (April 1994), where a $^{197}$Au target was bombarded with an E/A = 35 MeV $^{86}$Kr beam, the *SuperBall* was used in combination with the Washington University *Microball* charged-particle array. Data from this experiment are shown in Figs. VIII.6 to 8. Fig.VIII.6 exhibits contour diagrams of the correlations between multiplicity of neutrons ($m_n$) and charged-particle multiplicity ($m_{cp}$) (left panel) or

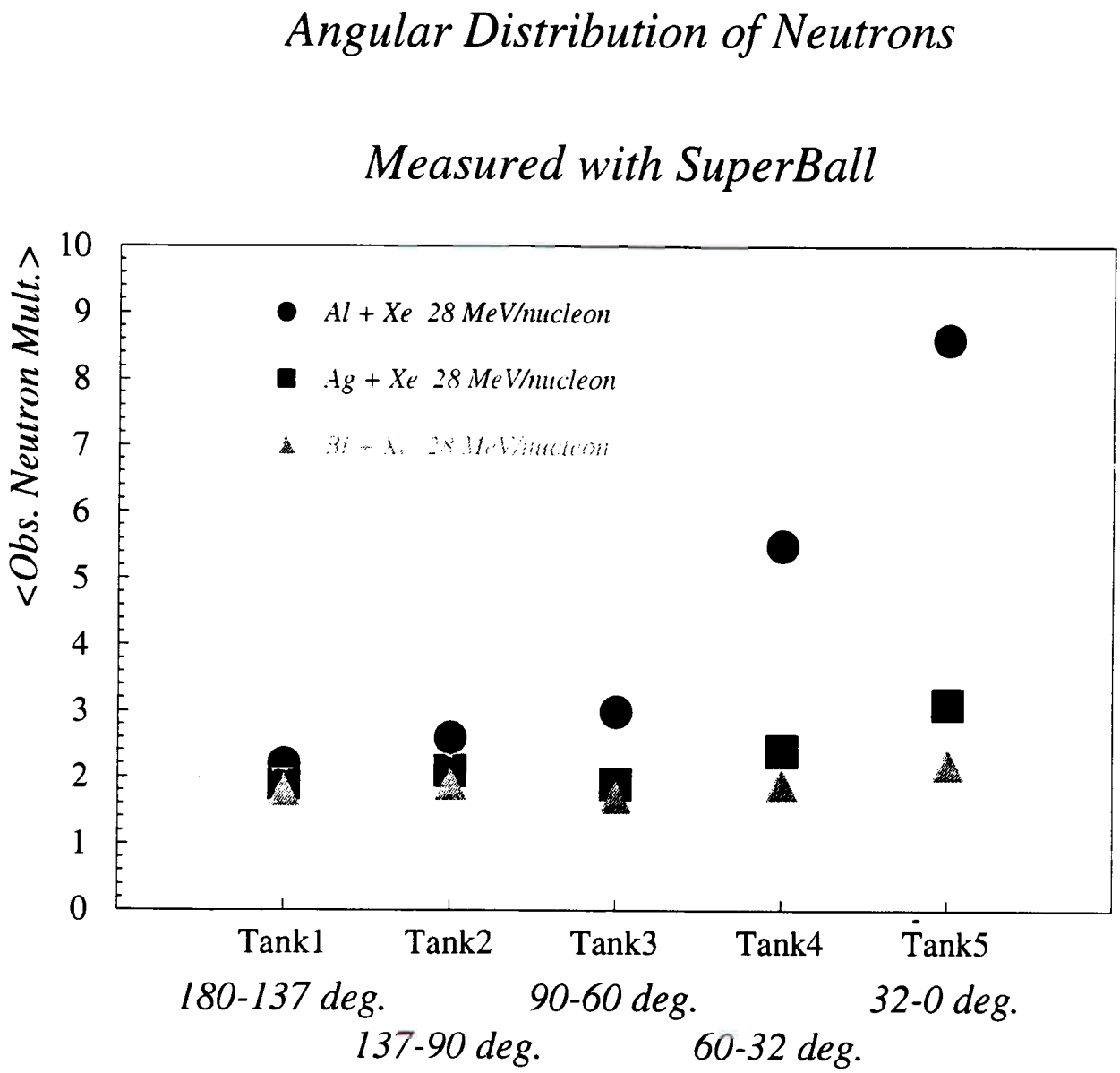


**Fig. VIII.5:** The observed neutron multiplicity is plotted *vs* the *SuperBall* segment number defining a coarse bin in laboratory angle.